

Polarization sensitive photodetector based on GaAsN

V. G. Ibarra-Sierra,¹ J. C. Sandoval-Santana,¹ R. S. Joshya,² H. Carrère,² L.A. Bakaleinikov,³
V. K. Kalevich,³ E. L. Ivchenko,³ X. Marie,² T. Amand,² A. Balocchi,² and A. Kunold¹

¹Área de Física Teórica y Materia Condensada, Universidad Autónoma Metropolitana

Azcapotzalco, Av. San Pablo 180, Col. Reynosa-Tamaulipas, 02200 Ciudad de México, México

²Université de Toulouse, INSA-CNRS-UPS, LPCNO, 135 avenue de Rangueil, 31077 Toulouse, France

³Ioffe Physical-Technical Institute, 194021 St. Petersburg, Russia

We propose and numerically simulate an optoelectronic compact circular polarimeter. It allows to electrically measure the degree of circular polarization and light intensity at room temperature for a wide range of incidence angles in a single shot. The device, being based on GaAsN, is easy to integrate into standard electronics and does not require bulky movable parts nor extra detectors. Its operation hinges mainly on two phenomena: the spin dependent capture of electrons and the hyperfine interaction between bound electrons and nuclei on Ga^{2+} paramagnetic centers in GaAsN. The first phenomenon confers the device with sensitivity to the degree of circular polarization and the latter allows to discriminate the handedness of the incident light.

I. INTRODUCTION

Just as frequency and intensity, polarization is one of the fundamental properties of light. In particular circular polarimetry, the determination of the degree of circular polarization, plays a determinant role in many recent technological developments. The capacity of circularly polarized light to interact with chiral biological structures has given rise to a wide range of applications that go from remote sensing of microbial organisms¹ to medical assessment techniques²⁻⁴. The detection of circularly polarized photon states is key to quantum information processing in the observation of entanglement between photons and electronic^{5,6} or nuclear^{7,8} spins.

The detection of circularly polarized light conventionally requires light to pass through a sequence of various hefty optical elements⁹ such as rotating polarizers and waveplates hampering the integration of circular polarimeters to standard electronics¹⁰. To circumvent the issues posed by standard circular polarimetry, many circular polarizer architectures have been proposed. Although organic photovoltaics¹¹ has allowed to build flexible and tunable full-Stokes polarimeters^{12,13} from naturally abundant materials, it requires the stacking of multiple components. The distinct optical response of plasmonic chiral metamaterials to left-handed (LCP) and right-handed (RCP) circularly polarized light has been exploited to realize circular polarizers^{10,14-17}. Despite the relative ease with which these structures can be merged with standard electronics¹⁴, they are limited by low circular polarization extinction ratios and low optical efficiency¹⁰ due to the losses of the parasitic currents generated in the nano-inclusions¹⁸. Regarding the compactness of the device, a major drawback of these structures is the requirement of off-chip detector to sense the scattered light¹⁸. Similar approaches have been taken in the use of chiral inclusions in dielectric metasurfaces¹⁶ and transition metal dichalcogenides¹⁹. Even though the more recent Fabry-Pérot cavity based polarimeters²⁰ can be, in principle, extended to circularly polarized light

measurements, so far they have only been demonstrated to have low signal-to-noise ratios under linearly polarized light. The silicon-on-insulator^{18,21,22} is probably the most robust platform for the integration of polarimeters with micro electronics because of their compatibility with metal oxide semiconductor fabrication process²².

Spin-optoelectronic devices employ the coupling of photon angular momentum and electron spin²³⁻²⁵. These devices rely on the photogeneration of spin-polarized conduction band electrons due to the unique optical selection rules of zinc-blende semiconductors under circularly polarized light. Through the spin-orbit interaction the light-polarization information can be translated first into an electron-spin polarization and then into an electrical signal via the inverse spin-Hall effect²³. Other similar alternatives convert the electron-spin polarization into a photo-voltage through the asymmetries in the electron motion due the built-in electric field induced by the Schottky contacts of the device²⁴. Inverse spin-Hall effect devices operate at room temperature²⁶ but allow only to detect the degree of circular polarization of light. In contrast, Schottky devices can detect simultaneously the degree of circular polarization and intensity in a single shot but are restricted to cryogenic temperatures.

In this paper we propose a spin-optoelectronic device for the simultaneous detection of the intensity and degree of circular polarization at room temperature. The detector is based on a GaAsN epilayer grown on GaAs. The detection scheme relies mainly on two phenomena: the generation of spin polarized conduction band (CB) electrons through optically oriented pumping and the spin dependent recombination (SDR)²⁷⁻⁵⁵ that the CB electrons undergo through Ga^{2+} paramagnetic centers^{35,39,44,54}. The orientation of the circularly polarized light (RCP or LCP) is discriminated from the sign of the so called Overhauser-like effective magnetic field^{29,45,49,50}.

The paper is organized as follows. Section II outlines how the incidence power and the degree of circular polarization affect the conductivity as a function of an applied magnetic field. The device architecture and the

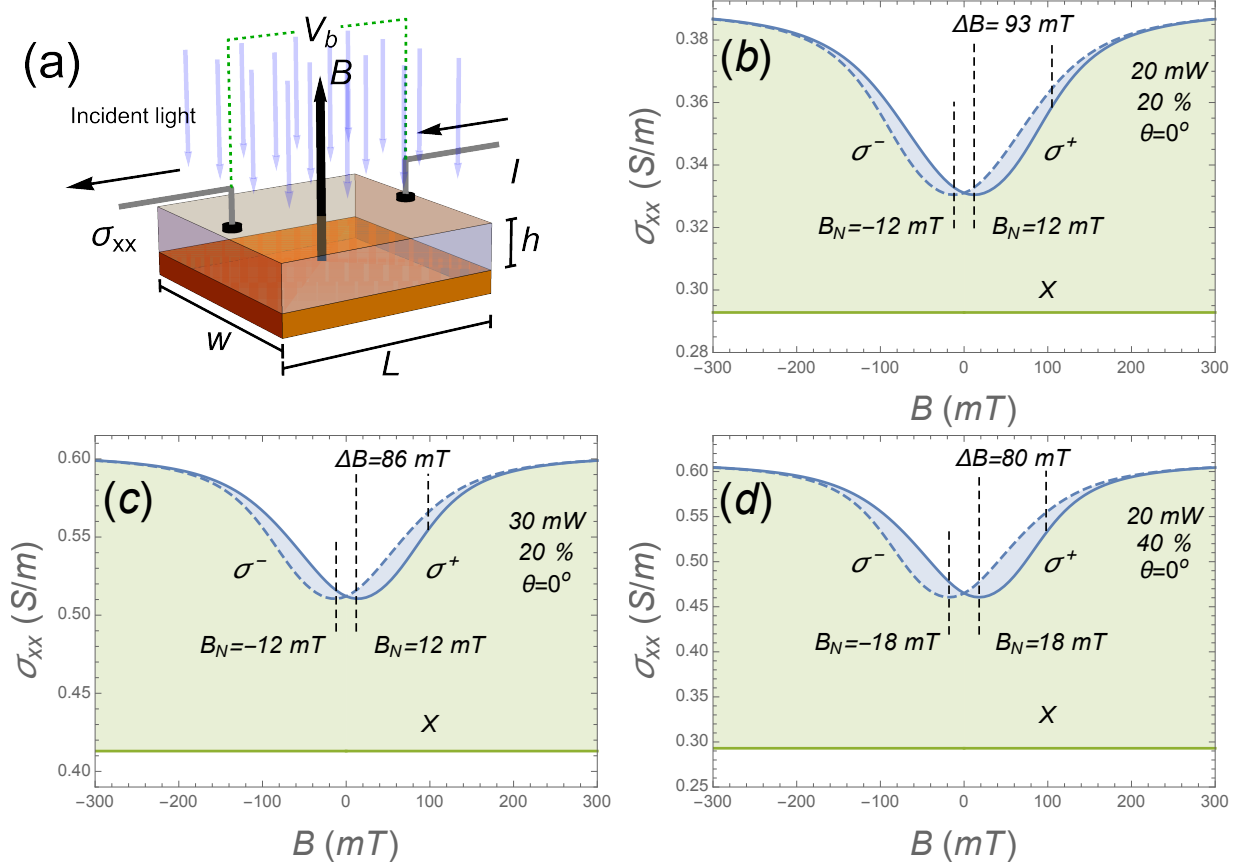


Figure 1. Longitudinal conductivity σ_{xx} as a function of the magnetic field in Faraday configuration ($\theta = 0^\circ$) for linearly (X), right circularly (σ^+) and left circularly (σ^-) polarized light. (a) Setup sketch of the GaAsN slab, magnetic field and incident light excitation. The magnetic field B is in Faraday configuration and the conductivity σ_{xx} is determined from the current i and the bias voltage V_b . The incident light power and the degree of circular polarization are set to (b) 20 mW and 20%, (c) 30 mW and 20% and (d) 20 mW and 40%.

procedure to deconvolve these quantities from the conductivity are sketched in Sec. III. Appendix A presents a detailed description of the model based on a master equation for the density matrix that permits the computation of the most relevant parameters to obtain the conductivity of the sample. In this same appendix we describe the method followed to fit the model parameters through measurements of the photoluminescence.

II. DETECTION OF THE DEGREE OF CIRCULAR POLARIZATION THROUGH THE SPIN FILTERING EFFECT

SDR produces an unbalance between the two CB electron spin polarization populations under circularly polarized light excitation. The unbalance is provoked by the different capture times that hinge on the relative spin orientation of CB electrons and Ga^{2+} center's bound electron^{34,35,41}. Whereas parallel-oriented spins block CB electrons from recombining, antiparallel ones promote recombination to the centers. This sets in motion a

spin filtering effect in which electrons with a given spin-orientation remain in the CB for long times, while those with the opposite spin polarization fastly recombine to the centers. Spin polarizations close to 100% can be attained after a few of these recombination cycles⁴⁹ at room temperature and over a wide wavelength excitation range⁵⁶. The generated spin-polarized CB electron excess population largely enhances the photo-conductivity under circularly polarized illumination as compared to linearly polarized one^{38,42}. A similar argument applies to the holes left behind by the photoexcited electrons. The spin-dependent photo-conductivity thus provides with the means to transduce the degree of electron spin polarization into an electrical signal.

Even though it can be modulated by the degree of spin polarization, the conductivity itself does not allow to discriminate between RCP and LCP light; it is insensitive to the spin direction of the excess CB electrons and, consequently, the circular polarization handedness of the incident light. However, the two handedness of circularly polarized light can be made to have a different effect on the Ga^{2+} centers by applying a relatively

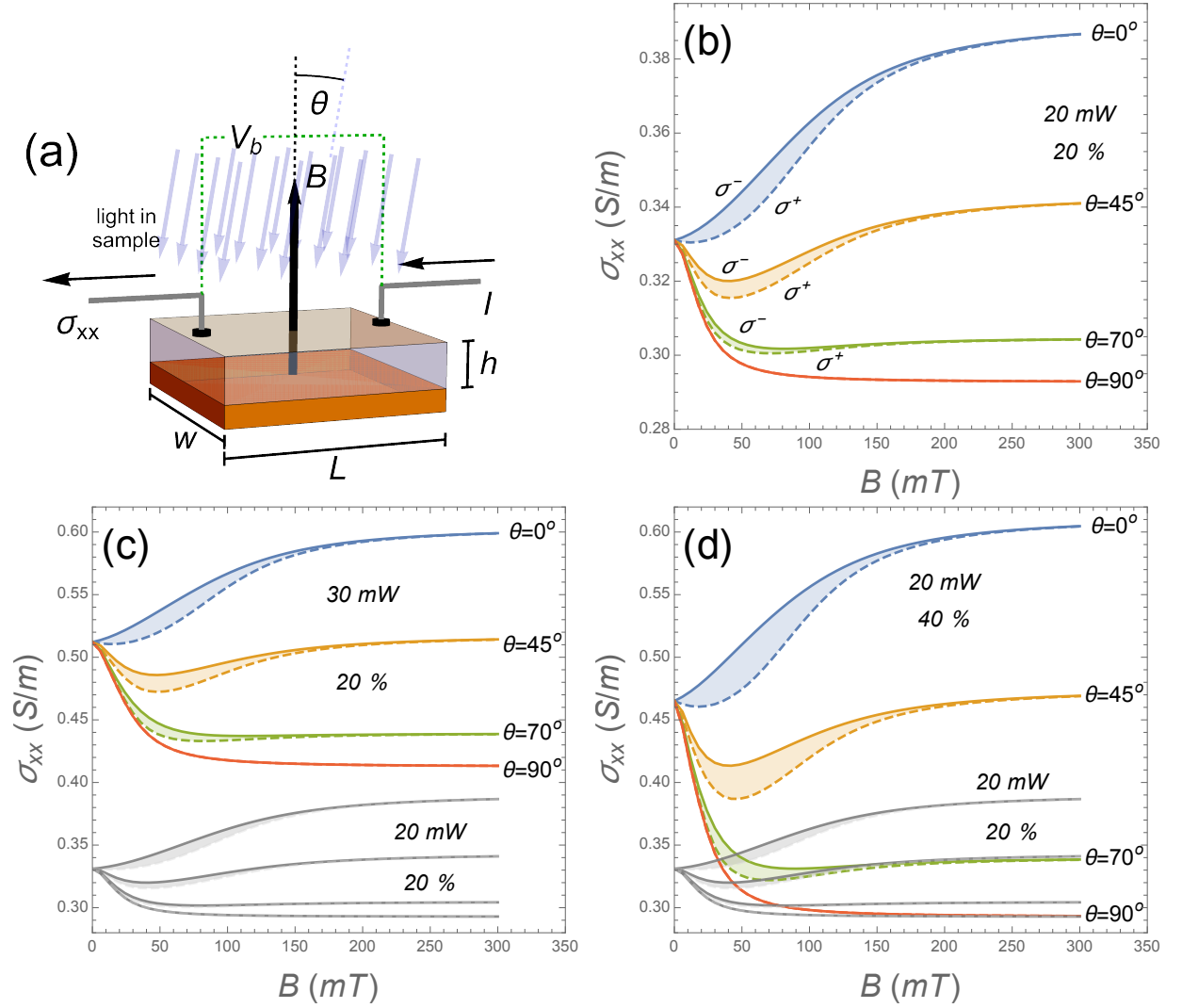


Figure 2. Longitudinal conductivity σ_{xx} as a function of the magnetic field for different relative angles, power intensities, degree and orientation of circularly polarized light. (a) Setup sketched of the GaAsN slab, magnetic field and incident light excitation. The relative angle θ between the magnetic field and the propagation direction of light inside the sample is marked above the magnetic field. The conductivity σ_{xx} is determined from the current i and the bias voltage V_b . Different incident light power and degree of circular polarization conditions are presented in the three panels: (b) 20 mW and 40% right circular polarization, (d) 30 mW and 40% right circular polarization and (d) 20 mW and 80% right circular polarization. Panels (b) and (c) show the plots of 20 mW and 40% right circular polarization for comparison. The solid and dashed lines correspond to σ^- (LCP) and σ^+ (RCP), respectively.

small magnetic field in Faraday configuration. This has primarily two effects: first, it amplifies the spin filtering effect^{43,45–47} and second, it generates an Overhauser-like magnetic field. The main cause of these two phenomena has been identified as the hyperfine interaction between the outer shell bound electron and the nucleus of the Ga^{2+} center^{46–49,51}. The amplification of the spin filtering effect gives the photoluminescence intensity as a function of the magnetic field the shape of an inverted Lorentzian function whose minimum is located at the Overhauser-like magnetic field^{29,45,49,50}. The position of this minimum, or more precisely, the sign of the Overhauser-like magnetic field are key to differentiating

between the two orientations of circularly polarized light. The Overhauser-like magnetic field is positive for RCP and negative for LCP.

Figure 1 shows plots of the calculated longitudinal conductivity σ_{xx} as a function of the magnetic field for linearly polarized light (X , green), right circularly polarized light (σ^+ , solid blue line) and left circularly polarized light (σ^- , dashed blue line). The electrical current is calculated through the Drude model. The setup is sketched in Fig. 1(a). We consider rectangular GaAsN slabs of length L , width w and height h subject to a perpendicular magnetic field B and a bias voltage V_b applied along the length L [see Fig. 1(a)]. The longitudinal component

of the conductivity is given by the sum of the electron, light hole and heavy hole contributions

$$\sigma_{xx} = e \left[\frac{\bar{n}\mu_e}{1 + \mu_e^2 B^2} + \frac{\bar{p}\mu_{lh}/2}{1 + \mu_{lh}^2 B^2} + \frac{\bar{p}\mu_{hh}/2}{1 + \mu_{hh}^2 B^2} + \frac{\left(\frac{\bar{n}\mu_e^2 B}{1 + \mu_e^2 B^2} - \frac{\bar{p}\mu_{lh}^2 B/2}{1 + \mu_{lh}^2 B^2} - \frac{\bar{p}\mu_{hh}^2 B/2}{1 + \mu_{hh}^2 B^2} \right)^2}{\frac{\mu_e \bar{n}}{1 + \mu_e^2 B^2} + \frac{\mu_{lh} \bar{p}/2}{1 + \mu_{lh}^2 B^2} + \frac{\mu_{hh} \bar{p}/2}{1 + \mu_{hh}^2 B^2}} \right], \quad (1)$$

where e is the electron charge, $\mu_e = 300 \text{ cm}^2/\text{Vs}$, $\mu_{lh} = 50 \text{ cm}^2/\text{Vs}$, and $\mu_{hh} = 50 \text{ cm}^2/\text{Vs}$ ^{57–62} are the electron, light hole and heavy hole mobilities. Naturally, the current intensity through a slab is given by

$$I = \sigma_{xx}(V_b/L)wh. \quad (2)$$

The electron and hole densities \bar{n} and \bar{p} , needed in the expressions above, are obtained from the quantum statistical averages of the density matrix (A31) and (A32). The density matrix is worked out from the numerical solution of a master equation previously developed by us⁶³. In Appendix A we present a detailed description of this method and list the input parameters. The second line of Eq. (1) comes from the transverse Hall field. These terms also introduce a magnetic field dependence in σ_{xx} , but they are far exceeded by the one introduced by \bar{n} and \bar{p} . Indeed, the inverted Lorentzian shape of this curve comes entirely from \bar{n} and \bar{p} as functions of the magnetic field. These curves strongly resemble the inverted Lorentzian obtained for the photoluminescence⁴³, a trait of the amplification of the spin filtering effect under a Faraday configuration magnetic field. This particular behaviour enters the conductivity in Eq. (1) through the electron and hole densities. We observe that the conductivity is enhanced when the illumination is switched to σ^+ or σ^- . This difference (green shaded region) permits to distinguish between linearly and circularly polarized incident light. One of the most significant characteristics of these plots is the different displacements created by σ^+ and σ^- incident light. While the incident RCP light shifts the Lorentzian curve 12 mT to the right, the LCP light shifts it to the left by the same amount. The contrast between these two curves (blue shaded region) allows to discriminate between RCP and LCP light. Comparing panel (b) with panels (c) and (d) we notice that either increasing the illumination power P_{exc} (from 20 mW to 30 mW), or its degree of circular polarization P_c (from 20% to 40%) appreciably changes some of the $\sigma_{xx}(B)$ features. Particular attention should be paid to the Overhauser-like magnetic field B_N and the Lorentzian width ΔB . These two quantities are known to be constant functions of the power intensity after they saturate^{45,63} at a threshold power which, in this case, is roughly 10 mW. Further on, this property of B_N and ΔB will be important to select the relevant parameters used to characterize some of the properties of light as incident power, degree of circular polarization and relative angle.

The incidence angle of circularly polarized light also has a strong impact on the conductivity of the sample.

A complete analysis of its multiple effects outside normal incidence would require to consider the variations of the intensity, propagation direction and the polarization predicted by the Fresnel equations and the Snell law. These depend on the widths of the GaAs cap, present in some architectures, and the GaAsN slab. This would, however, yield sample geometry dependent conductivities. So as to obtain data of a more general nature it is convenient to express our results in terms of the relative angle θ between the applied magnetic field and the propagation line of light inside the sample. Given its isotropy, the model (presented in Appendix A), is sensitive only to the relative orientation of the applied magnetic field and the propagation direction of light inside the sample. This reduces the number of used variables and considerably simplifies the discussion. Even though the angle θ has a noticeable effect on the conductivity it is still possible to carry out undistorted intensity and degree of circular polarization measurements. In Fig. 2 we observe the conductivity as a function of the magnetic field for angles between 0° (Faraday configuration) to 90° (Voigt configuration). A sketch of the setup is presented in Fig. 2 (a). We observe that at Faraday geometry ($\theta = 0$) the $\sigma_{xx}(B)$ adopts the features of the amplification of the spin filtering effect, namely, it takes the form of a downward Lorentzian-like curve shifted by B_N . Meanwhile, at Voigt geometry ($\theta = 90^\circ$), $\sigma_{xx}(B)$ takes the shape of the upward centered Lorentzian that characterizes the Hanle effect³⁶. At oblique angles the conductivity behaves as a combination of both downward and upward Lorentzians⁵⁰. In panel (b) we use as reference $\sigma_{xx}(B)$ under illumination with an incident power of 20 mW and a degree of circular polarization of 20%. The conductivity in panel (b) is contrasted with the conductivity calculated for an incident power of 30 mW in panel (c) and 40% degree of circular polarization in panel (d). We notice that even for very wide relative angles ($\theta \leq 70^\circ$) there is a clear distinction between σ^+ and σ^- . The most efficient detection configuration is at normal incidence where this difference is maximized. Further on we show that even at wide relative angles it is possible to measure the intensity and the degree of circular polarization.

From Fig. 1 it can then be said that in general the intensity, the degree of circular polarization and its handedness are encoded in $\sigma_{xx}(B)$. It still remains to find a way to deconvolve P_{exc} , P_c and θ from the conductivity. For this purpose we have defined the following two parameters

$$\Delta_1(B) = \sigma_{xx}(-B) + \sigma_{xx}(B), \quad (3)$$

$$\Delta_2(B) = \sigma_{xx}(-B) - \sigma_{xx}(B), \quad (4)$$

which are plotted in Fig. 3 as a function of the magnetic field. The parameter $\Delta_1(B)$ depends both on the incident power [panel (a)] and degree of circular polarization [panel (b)]. It is however insensitive to the orientation of the circular polarization. Additionally it is a fairly smooth function of the magnetic field and can therefore be expected to provide information on the power and the

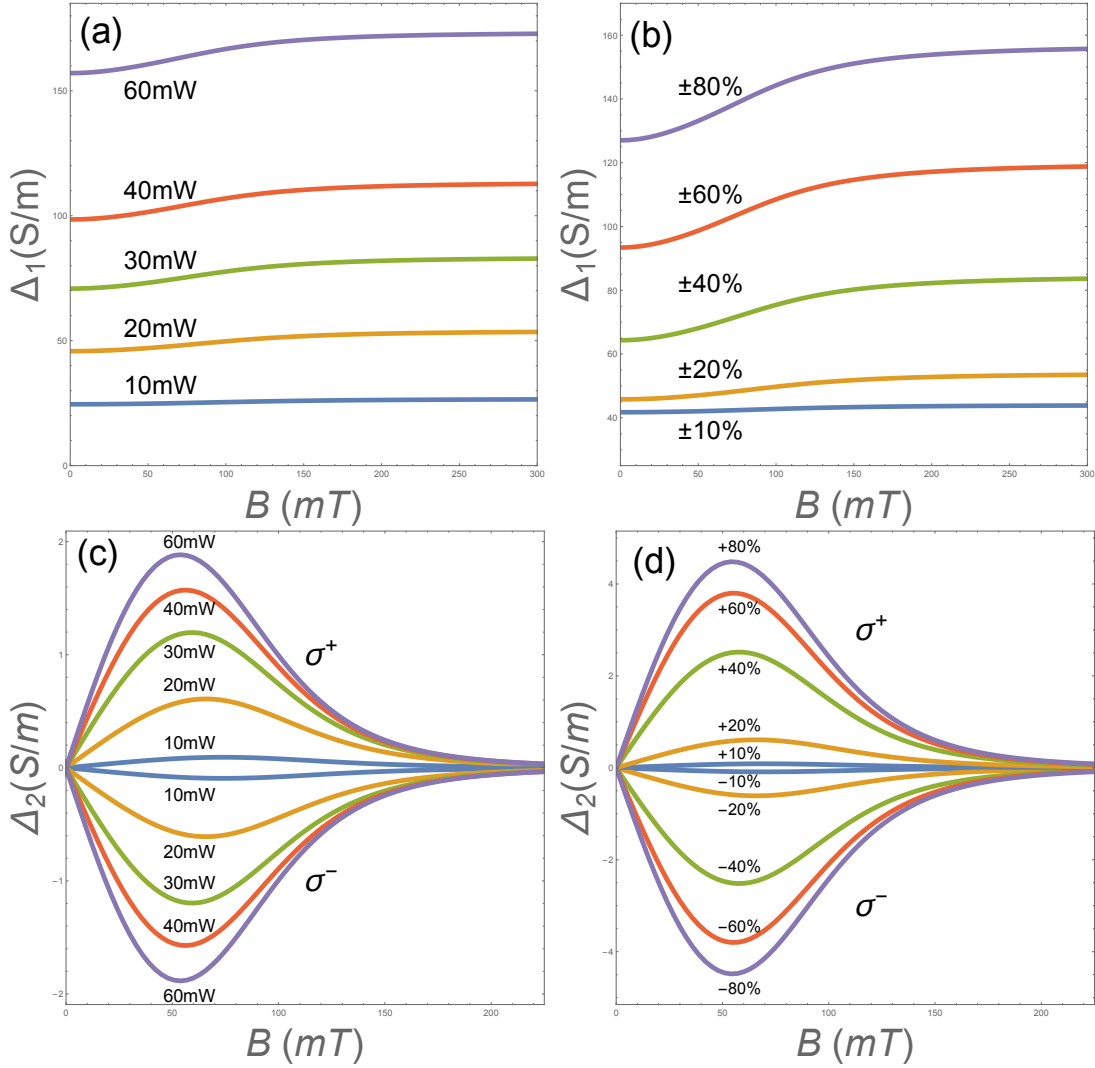


Figure 3. Parameters (a,b) $\Delta_1(B)$ and (c,d) $\Delta_2(B)$ as a function of the magnetic field for different incident powers (a,c) and degree of circular polarizations (b,d) for $P_{exc} = 20$ mW.

degree of circular polarization regardless of the applied magnetic field. Instead, $\Delta_2(B)$ has a pronounced sensitivity to power [panel (c)] and both degree of circular polarization [panel (c)] and its orientation [panels (c) and (d)] at approximately $B = 50$ mT. This value depends on B_N and ΔB which, as mentioned earlier, remain constant above a certain power threshold. Due to this, the maximum sensitivity of $\Delta_2(B)$ to power and degree of circular polarization always occurs at the same magnetic field value. The fact that both parameters are very sensitive at fixed values of the magnetic field is central to the design of the polarimeter architecture; not only no variable magnetic field is needed to characterize light, but its magnitude is small enough that it can be generated by small permanent magnets.

The previous results give us an inkling on what parameters may encode all the information necessary to characterize light's degree of circular polarization and

power. We know that at $B = 50$ mT $\Delta_1(B)$ and $\Delta_2(B)$ are strongly responsive to changes in power and degree of circular polarization. Moreover, the sign of $\Delta_2(50$ mT), being a measure of the asymmetry, provides information on the handedness of the degree of polarization. Thereby, a suitable set of parameters to fully characterize an incident beam of light is $\Gamma_1 = \Delta_1(50$ mT) and $\Gamma_2 = \Delta_2(50$ mT). In the next section we propose a device architecture that allows to measure these three parameters and explain how to extract from them the incidence power P_{exc} , the degree of circular polarization P_c and its handedness.

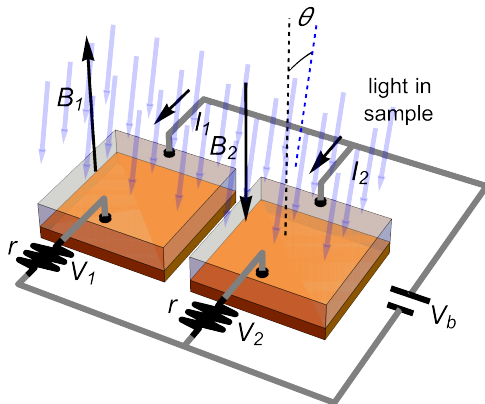


Figure 4. Schematics of the polarimeter. Both slabs are connected in parallel with a bias voltage source V_b . The voltages in the resistances r , V_1 and V_2 , are used to determine the current intensities I_1 and I_2 that travel through each GaAsN epilayer slab. The magnetic fields B_1 and B_2 are produced by the permanent magnets (dark blue) located on the base of each slab. The relative angle θ between the magnetic field and the propagation direction of light inside the sample is indicated.

III. DEVICE ARCHITECTURE AND DECONVOLUTION OF THE INCIDENT POWER, DEGREE OF POLARIZATION AND ITS ORIENTATION

The proposed device consists of interconnected slabs of $\text{GaAs}_{1-x}\text{N}_x$ as shown in Fig. 4. Each slab consists of a $\text{GaAs}_{1-x}\text{N}_x$ epilayer on a (100)-oriented semi-insulating GaAs substrate^{31,33}. This whole heterostructure is depicted as a transparent parallelepiped. The magnetic fields B_1 and B_2 are produced by permanent magnets beneath the GaAsN/GaAs heterostructures. The voltage source V_b is used to drive the currents I_1 and I_2 through the GaAsN slabs. The voltages V_1 and V_2 in the resistances r allow to detect the currents I_1 and I_2 . The permanent magnets sizes should be chosen as to generate the magnetic fields $B_1 = -B_2 = 50$ mT providing with enough information to obtain Γ_1 and Γ_2 . According to Eqs. (3) and (4) it would seem that three values of the conductivity [$\sigma_{xx}(0)$, $\sigma_{xx}(50 \text{ mT})$ and $\sigma_{xx}(-50 \text{ mT})$] are needed to obtain Γ_1 and Γ_2 . This would imply the need for an extra third slab of GaAsN. However, $\sigma_{xx}(0)$ can be estimated as $(\sigma_{xx}(50 \text{ mT}) + \sigma_{xx}(-50 \text{ mT}))/2$ restricting the number of slabs to two. An equivalent set-up would consist of a single slab of GaAsN where a microcoil would generate an alternating magnetic field.

Figures 5 and 6 show the power and degree of polar-

ization isolines on the $\Gamma_1 - \Gamma_2$ plane under σ^- and σ^+ illumination. Under normal incidence ($\theta = 0$) the degree of circular polarization P_c and the power P_{exc} can be determined by interpolating between the isolines in Figs. 5a or 6a depending on if $\Gamma_2 < 0$ (σ^-) or $\Gamma_2 > 0$ (σ^+). The progression of Figs. 5a, b, c and Figs. 6a, b, c, shows that despite the slight deformation due to the variation in the incidence angle, the isolines preserve their main topological properties. Moreover, it can be readily proven from the Fresnel equations, that the refracted light remains elliptically polarized even for incidence angles far from $\theta = 0^\circ$. Hence, the values of P_c and P_{exc} can be determined for a very wide range of incidence angles that approximately goes from $\theta = 0^\circ$ to $\theta = 50^\circ$.

IV. CONCLUSIONS

In summary, we have developed the concept of a spin-optoelectronic detector for the simultaneous measurement of the degree of circular polarization, its handedness and the intensity of a light excitation. We report on a theoretical analysis and numerical simulations based on a master equation approach that has been previously shown to yield very good quantitative agreement with experimental results shown in Fig. 7. This all-electronic compact device would operate at room temperature requiring no additional bulky movable parts. It relies on the unique spin selection rules of GaAs and spin-dependent capture of CB electrons that takes place through the Ga^{2+} centers in GaAsN. The hyperfine interaction that couples bound electrons and nuclei in the centers induces an asymmetry in the electron and hole population that is sensitive to the circular polarization orientation of the incident light. The device consists of two independent GaAsN based independent detectors each subject to different magnetic fields generated by small permanent magnets. The values of the magnetic fields are tuned to enhance the sensitivity of each detector to a given property of light. We expect that our proposed circular polarimeter will allow for the possibility of simultaneously detecting the intensity and the degree of circular polarization in an integrated optoelectronic platform.

V. ACKNOWLEDGEMENTS

We acknowledge funding from LIA CNRS-Ioffe RAS ILNACS. A.K., J.C.S.S. and V.G.I.S. gratefully appreciate the financial support of Departamento de Ciencias Básicas UAM-A grant numbers 2232214 and 2232215. X.M. also thanks Institut Universitaire de France. This work was supported by Programme Investissements d'Avenir under the program ANR-11-IDEX-0002-02, reference ANR-10-LABEX-0037-NEXT.

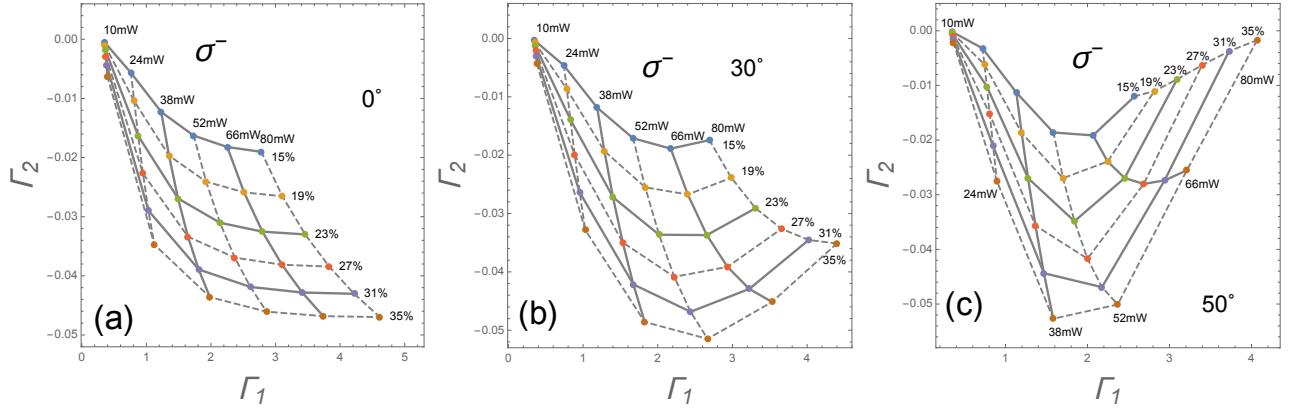


Figure 5. Power and degree of circular polarization isolines as a function of $\Gamma_1 = \Delta_1(50\text{mT})$ and $\Gamma_2 = \Delta_2(50\text{mT})$ under σ^- illumination at a relative angle of (a) 0° , (b) 30° and (c) 50° .

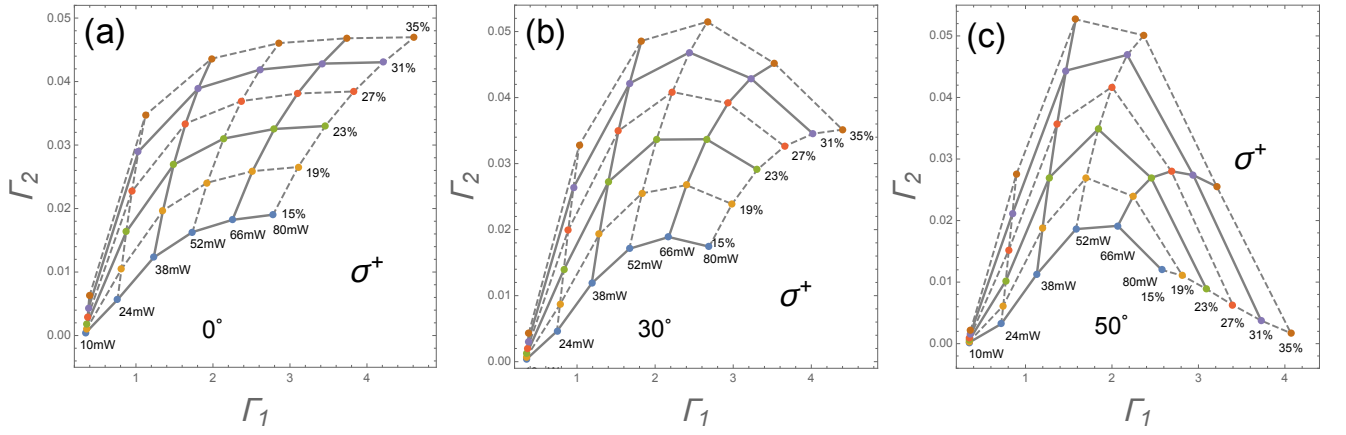


Figure 6. Power and degree of circular polarization isolines as a function of Γ_1 and Γ_2 under σ^+ illumination at a relative angle of (a) 0° , (b) 30° and (c) 50° .

Appendix A: Model

In this appendix we present a summary of the method used for the computation of the quantum statistical averages of the electron and hole populations \bar{n} and \bar{p} , necessary to obtain the conductivity σ_{xx} . For a detailed presentation of this method see Ref. [63].

Any quantum statistical average may be obtained from the trace of density matrix multiplied by the appropriate operator. The density matrix ρ , in turn, is ensued from the master equation⁶³

$$\frac{d\rho}{dt} = \frac{i}{\hbar} [\rho, H] + \mathcal{D}(\rho), \quad (\text{A1})$$

where H is the Hamiltonian and \mathcal{D} is the dissipator.

The density matrix may be expressed as the direct sum

$$\rho = \rho_v \oplus \rho_c \oplus \rho_1 \oplus \rho_2, \quad (\text{A2})$$

where ρ_v and ρ_c are the density submatrices for valence band and conduction band electrons respectively. The density submatrices ρ_1 and ρ_2 correspond to singly and

double occupied Ga^{2+} centers. The density matrix, as any other matrix relevant to (A1), can be conveniently expanded in terms of the elements of an internal space of Hermitian matrices⁶³

$$\Lambda = \{p, S_k, U_{k,j,i}, V_{j,i},\} = \{\lambda_1, \lambda_2, \dots, \lambda_d\}, \quad i, j, k = 0, 1, 2, 3, \quad d = 85, \quad (\text{A3})$$

where

$$p = 1_{1 \times 1} \oplus 0_{2 \times 2} \oplus 0_{8 \times 8} \oplus 0_{4 \times 4}, \quad (\text{A4})$$

$$S_k = 0_{1 \times 1} \oplus (s_k) \oplus 0_{8 \times 8} \oplus 0_{4 \times 4}, \quad (\text{A5})$$

$$U_{k,j,i} = 0_{1 \times 1} \oplus 0_{2 \times 2} \oplus (s_k \otimes s_j \otimes s_i) \oplus 0_{4 \times 4}, \quad (\text{A6})$$

$$V_{j,i} = 0_{1 \times 1} \oplus 0_{2 \times 2} \oplus 0_{8 \times 8} \oplus (s_j \otimes s_i), \quad (\text{A7})$$

with $i, j, k = 0, 1, 2, 3$. Here, $s_0 = 1_{2 \times 2}/2$ where $1_{2 \times 2}$ is the 2×2 identity matrix and $s_{1,2,3}$ are the spin matrices following the standard commutation rules

$$[s_i, s_j] = i\hbar \sum_k \epsilon_{i,j,k} s_k, \quad i, j, k = 1, 2, 3. \quad (\text{A8})$$

This particular choice of a matrix basis is advantageous for a number of reasons. First, any operator can be ex-

pressed as a linear combination of the elements of Λ . Second, its elements are orthogonal with respect to the trace,

$$\text{tr} [\lambda_q^\dagger \lambda_{q'}] = \text{tr} [\lambda_q^2] \delta_{q,q'}, \quad (\text{A9})$$

which is related to the quantum statistical average of physical observables. Of particular importance are the quantum statistical averages of the elements of Λ ,

$$\bar{\lambda}_q = \text{Tr} [\rho \lambda_q], \quad (\text{A10})$$

whereby the density matrix can be expanded as

$$\rho = \sum_{q=1}^d \frac{\bar{\lambda}_q \lambda_q}{\text{Tr} [\lambda_q^2]} = \frac{\bar{p} p}{\text{Tr} [p^2]} + \sum_{k=0}^3 \frac{\bar{S}_k S_k}{\text{Tr} [S_k^2]} + \sum_{k,j,i=0}^3 \frac{\bar{U}_{k,j,i} U_{k,j,i}}{\text{Tr} [U_{k,j,i}^2]} + \sum_{j,i=0}^3 \frac{\bar{V}_{j,i} V_{j,i}}{\text{Tr} [V_{j,i}^2]}. \quad (\text{A11})$$

In general, any operator O can be expanded in this basis as

$$O = \sum_{q=1}^d \frac{\text{Tr} [O \lambda_q]}{\text{Tr} [\lambda_q^2]} \lambda_q = \frac{\text{Tr} [O p]}{\text{Tr} [p^2]} p + \sum_{k=0}^3 \frac{\text{Tr} [O S_k]}{\text{Tr} [S_k^2]} S_k + \sum_{k,j,i=0}^3 \frac{\text{Tr} [O U_{k,j,i}]}{\text{Tr} [U_{k,j,i}^2]} U_{k,j,i} + \sum_{j,i=0}^3 \frac{\text{Tr} [O V_{j,i}]}{\text{Tr} [V_{j,i}^2]} V_{j,i}, \quad (\text{A12})$$

and its corresponding quantum statistical average is given by

$$\bar{O} = \text{Tr} [O \rho] = \sum_{q=1}^d \frac{\text{Tr} [O \lambda_q]}{\text{Tr} [\lambda_q^2]} \bar{\lambda}_q. \quad (\text{A13})$$

In this way, the density of VB holes is represented by the matrix p , the density of CB electrons by $n = 2S_0$, the spin components of CB electrons by S_k ($k = 1, 2, 3$), the concentration of singly occupied traps by $N_1 = 8U_{0,0,0}$, the spin components of bound electrons in Ga^{2+} centers by $S_{ck} = 4U_{k,0,0}$ ($k = 1, 2, 3$) and the concentration of doubly occupied traps by $N_2 = 4V_{0,0}$. Using (A12) we can also decompose more complicated operators. For instance, the components of the nuclear spin operators of singly charged centers \mathbf{I}_1 and doubly charged centers \mathbf{I}_2 can readily be expressed as a superposition of the elements of (A3) by

$$I_{1,k} = \sum_{j,i=0}^3 \frac{\text{Tr} [I_{1,k} U_{0,j,i}]}{\text{Tr} [U_{0,j,i} U_{0,j,i}]} U_{0,j,i}, \quad (\text{A14})$$

$$I_{2,k} = \sum_{j,i=0}^3 \frac{\text{Tr} [I_{2,k} V_{j,i}]}{\text{Tr} [V_{j,i} V_{j,i}]} V_{j,i}. \quad (\text{A15})$$

Note that in the previous expressions only a few elements of the basis are needed.

The Hamiltonian in (A1)

$$H = \hbar \boldsymbol{\omega} \cdot \mathbf{S} + \hbar \boldsymbol{\Omega} \cdot \mathbf{S}_c + A \mathbf{I}_1 \cdot \mathbf{S}_c, \quad (\text{A16})$$

accounts for the Zeeman and hyperfine interactions. The first two terms correspond to the Zeeman interaction of an external magnetic field \mathbf{B} with the CB electrons spin \mathbf{S} and the centers bound electrons spin \mathbf{S}_c . In these expressions $\boldsymbol{\omega} = g\mu_B \mathbf{B}/\hbar$, $\boldsymbol{\Omega} = g_c\mu_B \mathbf{B}/\hbar$, where μ_B is the Bohr magneton, g is the gyromagnetic factor for CB electrons and $g_c = 2^{51}$ is the gyromagnetic factor for bound electrons in singly occupied centers. The third term is responsible for the hyperfine interaction that takes place in singly occupied centers between the bound electron spin \mathbf{S}_c and the nuclear spin \mathbf{I}_1 . The hyperfine parameter is A . In doubly occupied traps electrons form a singlet state that does not interact with the nuclear spin \mathbf{I}_2 .

The dissipator

$$\mathcal{D}(\rho) = \mathcal{G} + \mathcal{D}_S + \mathcal{D}_{SC} + \mathcal{D}_1 + \mathcal{D}_2 + \mathcal{D}_{SDR} + \mathcal{D}_P, \quad (\text{A17})$$

is primarily composed of generation (\mathcal{G}), spin relaxation (\mathcal{D}_S and \mathcal{D}_{SC} , \mathcal{D}_1 and \mathcal{D}_2) and recombination terms (\mathcal{D}_{SDR} and \mathcal{D}_P). The electron-hole pair generating term is given by

$$\mathcal{G} = (G_+ + G_-)(p + n) + 2(G_+ - G_-)\mathbf{e} \cdot \mathbf{S}, \quad (\text{A18})$$

where \mathbf{e} is a unitary vector in the excitation direction. Spin-up and spin-down CB electron generation rates are given by the smooth step function

$$G(t)_{\pm} = \frac{G_0 P_{exc}}{2} \frac{1 \pm P_e}{2} \left[1 + \tanh \left(\frac{t - t_0}{\Delta t} \right) \right], \quad (\text{A19})$$

where P_{exc} is the excitation power, G_0 is the power to generation factor, Δt is the width of the step function and the spin polarization degree is parametrized by $P_e \in [-1, 1]$.

The electronic and nuclear spin relaxation dissipators are in general derived from Wangsness - Bloch - Redfield theory^{51,64-66}. The dissipator for CB electrons straightforwardly gives

$$\mathcal{D}_S = -\frac{1}{2\tau_s} \sum_{k=1}^3 [S_k, [S_k, \rho]]. \quad (\text{A20})$$

The spin relaxation dissipators in centers require closer attention. Firstly, in singly occupied centers it is important to distinguish two different electronic and nuclear relaxation times: one belonging to the electronic and nuclear spins themselves and the other to the correlation between electronic and nuclear spins⁶³. These two times are quite different in magnitude. Secondly, in singly and doubly occupied traps, we assume that dipole-dipole interaction between centers and neighbouring Ga atoms is the leading mechanism of nuclear spin relaxation⁵¹. The dissipator for the bound electron spin can thus be ex-

panded in terms of the Λ subbasis elements corresponding to the singly occupied traps

$$\mathcal{D}_{SC} = -\frac{1}{2\tau_{sc}} \sum_{k=1}^3 \frac{\text{Tr}[\Gamma_S U_{k,0,0}]}{\text{Tr}[U_{k,0,0} U_{k,0,0}]} U_{k,0,0} - \frac{1}{2\tau_{sco}} \sum_{k,j,i=0}^3 \mu_{k,j,i} \frac{\text{Tr}[\Gamma_S U_{k,j,i}]}{\text{Tr}[U_{k,j,i} U_{k,j,i}]} U_{k,j,i}, \quad (\text{A21})$$

where

$$\Gamma_S = \sum_{k=1}^3 [S_{ck}, [S_{ck}, \rho]] \quad (\text{A22})$$

is the usual commutator arising from Wangsness - Bloch - Redfield theory for dipole-dipole interaction. The first line of (A21) is the projection of Γ_S on to the electron spin subbasis of Λ , namely, the spin components of the bound electron $S_{ck} = 4U_{k,0,0}$ for $k = 1, 2, 3$. Accordingly, the second line of (A21) is the projection of Γ_S on to the subbasis of electron-nucleus correlations which are selected by

$$\mu_{k,j,i} = \begin{cases} 0, & k = 0 \vee (k \neq 0 \wedge j = 0 \wedge i = 0) \\ 1, & k \neq 0 \wedge (j \neq 0 \vee i \neq 0) \end{cases}. \quad (\text{A23})$$

Each one of these projections is governed by a different relaxation time: τ_{sc} is the centers' electronic spin relaxation time and τ_{sco} is the relaxation time of correlations⁶³. Similarly, the nuclear spin relaxation dissipator is expanded as

$$\mathcal{D}_1 = -\frac{1}{3\tau_{n1}} \sum_{k=1}^3 \frac{\text{Tr}[\Gamma_I U_{k,0,0}]}{\text{Tr}[U_{k,0,0} U_{k,0,0}]} U_{k,0,0} - \frac{1}{2\tau_{n1co}} \sum_{k,j,i=0}^3 \mu_{k,j,i} \frac{\text{Tr}[\Gamma_I U_{k,j,i}]}{\text{Tr}[U_{k,j,i} U_{k,j,i}]} U_{k,j,i}, \quad (\text{A24})$$

where

$$\Gamma_I = \sum_{k=1}^3 [I_{1k}, [I_{1k}, \rho]] \quad (\text{A25})$$

comes out of the dipole-dipole interaction between the centers nuclear spin and the neighbouring Ga nuclei. The dissipator of doubly occupied centers reads

$$\mathcal{D}_2 = -\frac{1}{3\tau_{n2}} \sum_{k=1}^3 [I_{2k}, [I_{2k}, \rho]]. \quad (\text{A26})$$

Since in doubly occupied centers both electrons residing in the 4s orbital form a singlet state which is not correlated to the nuclear spin, \mathcal{D}_2 needs not be separated into the spin and correlation parts.

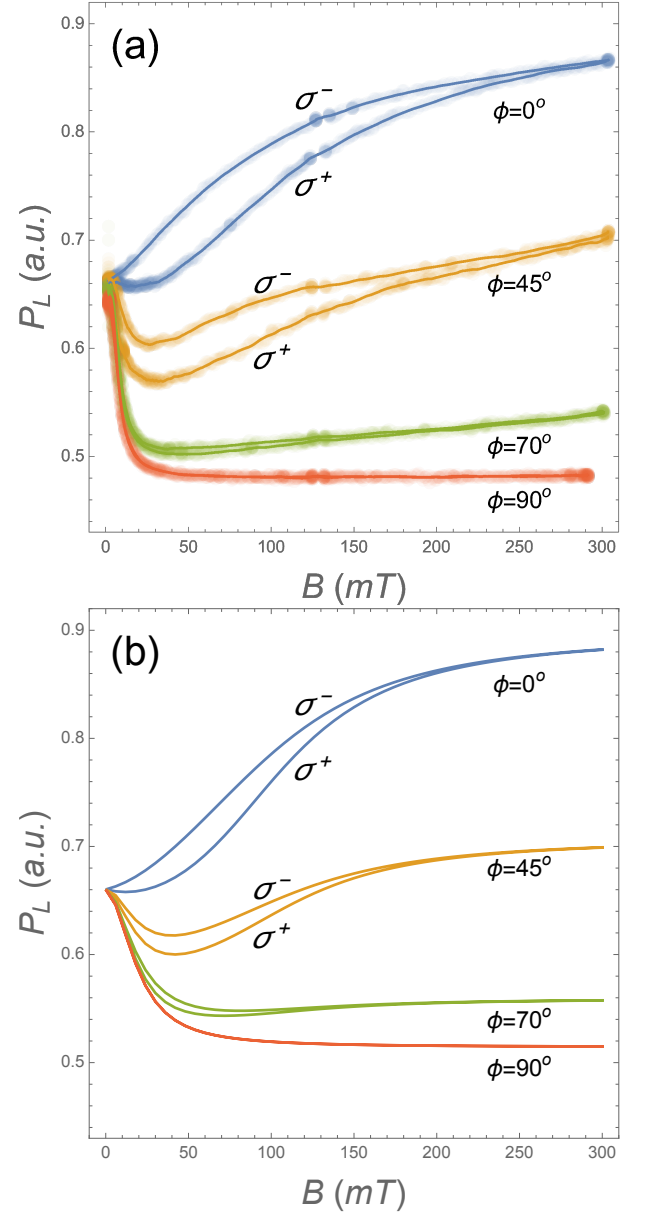


Figure 7. (a) Experimental and (b) theoretical results for the photoluminescence P_L as a function of an oblique magnetic field at an incident power of 20mW. The magnetic field is rotated from Faraday ($\phi = 0^\circ$) to Voigt ($\phi = 90^\circ$) configuration. In panel (a) the dots correspond to the experimental results and the solid lines are a guide to the eye.

The spin selective capture of electrons into singly oc-

cupied centers is accounted for by the dissipator⁶³

$$\begin{aligned} \mathcal{D}_{SDR} = & -2 \sum_{k=0}^3 \left(4c_n \sum_{k',k''=0}^3 \bar{S}_{k'} Q_{k,k',k''}^\top \bar{U}_{k'',j,i} \right) S_k \\ & - 8 \sum_{k,j,i=0}^3 \mu_{k,j,i} \left(c_n \sum_{k',k''=0}^3 \bar{S}_{k'} Q_{k,k',k''}^\top \bar{U}_{k'',j,i} \right) U_{k,j,i} \\ & + 4 \sum_{j,i=0}^3 \left(2c_n \sum_{k',k''=0}^3 \bar{S}_{k'} Q_{0,k',k''}^\top \bar{U}_{k'',j,i} \right) V_{j,i}, \quad (\text{A27}) \end{aligned}$$

where the capture coefficient of CB electrons $c_n = 1/N_0\tau^*$, τ^* is the electron recombination time in the low excitation power regime and N_0 is the total number of centers in the sample. The matrices $Q_{k,k',k''} = (Q_k)_{k',k''}$, related to the space rotations generators⁶⁷, are responsible for the spin dependent capture. These are defined by

$$\begin{aligned} Q_0 &= \begin{pmatrix} 1 & 0 & 0 & 0 \\ 0 & -1 & 0 & 0 \\ 0 & 0 & -1 & 0 \\ 0 & 0 & 0 & -1 \end{pmatrix}, \quad Q_1 = \begin{pmatrix} 0 & 1 & 0 & 0 \\ -1 & 0 & 0 & 0 \\ 0 & 0 & 0 & 0 \\ 0 & 0 & 0 & 0 \end{pmatrix}, \\ Q_2 &= \begin{pmatrix} 0 & 0 & 1 & 0 \\ 0 & 0 & 0 & 0 \\ -1 & 0 & 0 & 0 \\ 0 & 0 & 0 & 0 \end{pmatrix}, \quad Q_3 = \begin{pmatrix} 0 & 0 & 0 & 1 \\ 0 & 0 & 0 & 0 \\ 0 & 0 & 0 & 0 \\ -1 & 0 & 0 & 0 \end{pmatrix}. \quad (\text{A28}) \end{aligned}$$

Note that while Q_0 remains invariant under rotations, Q_1 , Q_2 and Q_3 rotate as the components of a three-dimensional vector.

The recombination of VB holes into doubly occupied centers is governed by the dissipator⁶³

$$\begin{aligned} \mathcal{D}_P = & - (4c_p \bar{p} \bar{V}_{0,0}) p + \frac{1}{8} \left(\frac{1}{2} \sum_{j,i=0}^3 \bar{p} \bar{U}_{0,j,i} \right) U_{0,j,i} \\ & - \frac{1}{4} \left(\sum_{j,i=0}^3 \bar{p} \bar{V}_{j,i} \right) V_{j,i}, \quad (\text{A29}) \end{aligned}$$

where $c_p = 1/N_0\tau_h$ is the capture coefficient for holes and τ_h is the hole recombination time in the high excitation power regime.

Having established the components of the master equation we now turn our attention to the determination of

the time dependence of observables such as \bar{n} and \bar{p} . Instead of directly solving the system of ordinary differential equations arising from A1 for the matrix elements of ρ , we work out the system of ordinary differential equations for the statistical averages of the elements of Λ . This procedure yields $d = 85$ differential equations of the form

$$\frac{d\bar{\lambda}_q}{dt} = \frac{i}{\hbar} \text{Tr} [[H, \lambda_q] \rho] + \text{Tr} [\mathcal{D}(\rho) \lambda_q]. \quad (\text{A30})$$

These are solved numerically over a sufficiently long time ($\approx 400\text{ns}$) to allow steady state conditions to be reached. Finally, the quantum average of any operator can be computed from the decomposition (A13). In particular, the CB electron and VB hole densities are

$$\bar{n} = \sum_{q=1}^d \frac{\text{Tr} [n \lambda_q]}{\text{Tr} [\lambda_q^2]} \bar{\lambda}_q, \quad (\text{A31})$$

$$\bar{p} = \sum_{q=1}^d \frac{\text{Tr} [p \lambda_q]}{\text{Tr} [\lambda_q^2]} \bar{\lambda}_q. \quad (\text{A32})$$

In order for the model to yield quantitatively realistic results, we have fitted its parameters using experimental measurements of the photoluminescence for various incident powers and magnetic field orientations. Varying the magnetic field orientation provides a complete set of experimental points, especially useful to determine the electronic and nuclear spin relaxation times τ_h , τ_r , τ^* , τ_s , τ_{sc} , τ_{sco} , τ_{n1} , τ_{n1co} and τ_{n2} . The photoluminescence, on the other hand, yields information on the power to generation factor G_0 and the overall number of paramagnetic centers $N_c = N_1 + N_2$ in the sample. The photoluminescence measurements were performed on a 100 nm thick GaAs_{1-x}N_x epilayer ($x = 0.021$) grown by molecular beam epitaxy on a (001) semi-insulating GaAs substrate and capped with 10 nm GaAs. The room temperature epilayer gap is 1080 nm. The excitation light was provided by a 850 nm laser diode. Figure 7 shows a comparison between the measured and the theoretical photoluminescence at an incident power of 20 mW. The model was also fitted using different incident powers which are not shown in this figure. The parameters that best fit experimental results on photoluminescence are $G_0 = 3 \times 10^{23} \text{cm}^{-3} \text{mW}^{-1}$, $\Delta t = 10 \text{ps}$, $N_c = N_1 + N_2 = 2.2 \times 10^{15} \text{cm}^{-3}$, $\tau_h = 20 \text{ps}$, $\tau_r = 1.4 \text{ns}$, $\tau^* = 10 \text{ps}$, $\tau_s = 120 \text{ps}$, $\tau_{sc} = 2 \text{ns}$, $\tau_{sco} = 18 \text{ns}$, $\tau_{n1} = 2 \text{ns}$, $\tau_{n1co} = 8 \text{ns}$, $\tau_{n2} = 100 \text{ps}$, $A = 0.069 \text{cm}^{-1}$ ⁴⁶, $g = 1$ and $g_c = 2$ ^{51,63}.

¹ W. B. Sparks, T. A. Germer, and R. M. Sparks, Publications of the Astronomical Society of the Pacific **131**, 075002 (2019).

² P. Whittaker, R. Kloner, D. Boughner, and J. Pickering, Basic research in cardiology **89**, 397 (1994).

³ D. C. Louie, L. Tchvialeva, S. Kalia, H. Lui, and T. K. Lee, in *Photonics in Dermatology and Plastic Surgery 2018*, Vol. 10467, edited by B. Choi and H. Zeng, International Society for Optics and Photonics (SPIE, 2018) pp. 44 – 52.

⁴ J. Chang, H. He, Y. Wang, Y. Huang, X. Li, C. He, R. Liao,

- N. Zeng, S. Liu, and H. Ma, *Journal of Biomedical Optics* **21**, 1 (2016).
- ⁵ W. Gao, P. Fallahi, E. Togan, J. Miguel-Sánchez, and A. Imamoglu, *Nature* **491**, 426 (2012).
 - ⁶ M. K. Bhaskar, R. Riedinger, B. Machielse, D. S. Levonian, C. T. Nguyen, E. N. Knall, H. Park, D. Englund, M. Lončar, D. D. Sukachev, *et al.*, *Nature* **580**, 60 (2020).
 - ⁷ E. Togan, Y. Chu, A. S. Trifonov, L. Jiang, J. Maze, L. Childress, M. G. Dutt, A. S. Sørensen, P. Hemmer, A. S. Zibrov, *et al.*, *Nature* **466**, 730 (2010).
 - ⁸ D. D. B. Rao, S. Yang, and J. Wrachtrup, *Phys. Rev. B* **92**, 081301(R) (2015).
 - ⁹ H. G. Berry, G. Gabrielse, and A. E. Livingston, *Appl. Opt.* **16**, 3200 (1977).
 - ¹⁰ A. Basiri, X. Chen, J. Bai, P. Amrollahi, J. Carpenter, Z. Holman, C. Wang, and Y. Yao, *Light: Science & Applications* **8**, 1 (2019).
 - ¹¹ O. Awartani, M. W. Kudenov, and B. T. O'Connor, *Applied Physics Letters* **104**, 093306 (2014), <https://doi.org/10.1063/1.4868041>.
 - ¹² S. G. Roy, O. M. Awartani, P. Sen, B. O'Connor, and M. W. Kudenov, *Opt. Express* **24**, 14737 (2016).
 - ¹³ R. Yang, P. Sen, B. T. O'Connor, and M. W. Kudenov, *Appl. Opt.* **56**, 1768 (2017).
 - ¹⁴ J. Bai, C. Wang, X. Chen, A. Basiri, C. Wang, and Y. Yao, *Photon. Res.* **7**, 1051 (ts, doi = 10.1364/PRJ.7.001051).
 - ¹⁵ M. Akbari, J. Gao, and X. Yang, *Opt. Express* **26**, 21194 (2018).
 - ¹⁶ J. Hu, X. Zhao, Y. Lin, A. Zhu, X. Zhu, P. Guo, B. Cao, and C. Wang, *Scientific Reports* **7**, 41893 (2017).
 - ¹⁷ Y. Zhao, M. Belkin, and A. Alù, *Nature communications* **3**, 1 (2012).
 - ¹⁸ Z. Lin, L. Rusch, Y. Chen, and W. Shi, *Opt. Express* **27**, 4867 (2019).
 - ¹⁹ Q. Jiang, B. Du, M. Jiang, D. Liu, Z. Liu, B. Li, Z. Liu, F. Lin, X. Zhu, and Z. Fang, *Nanoscale* **12**, 5906 (2020).
 - ²⁰ L. P. Stoevelaar, J. Berzinš, F. Silvestri, S. Fasold, K. Z. Kamali, H. Knopf, F. Eilenberger, F. Setzpfandt, T. Pertsch, S. M. B. Bäumer, and G. Gerini, *Opt. Express* **28**, 19818 (2020).
 - ²¹ W. Wu, Y. Yu, W. Liu, and X. Zhang, *Nanophotonics* **8**, 467 (01 Mar. 2019).
 - ²² J. Dong and H. Zhou, *Optics Communications* **465**, 125598 (2020).
 - ²³ K. Ando, M. Morikawa, T. Trypiniotis, Y. Fujikawa, C. H. W. Barnes, and E. Saitoh, *Applied Physics Letters* **96**, 082502 (2010), <https://doi.org/10.1063/1.3327809>.
 - ²⁴ S. K. Khamari, S. Porwal, S. M. Oak, and T. K. Sharma, *Applied Physics Letters* **107**, 072108 (2015), <https://doi.org/10.1063/1.4929326>.
 - ²⁵ E. L. Ivchenko and S. D. Ganichev, "Spin-dependent photogalvanic effects (a review)," (2017), [arXiv:1710.09223](https://arxiv.org/abs/1710.09223) [cond-mat.mes-hall].
 - ²⁶ E. Saitoh, M. Ueda, H. Miyajima, and G. Tatara, *Applied Physics Letters* **88**, 182509 (2006), <https://doi.org/10.1063/1.2199473>.
 - ²⁷ D. J. Lepine, *Phys. Rev. B* **6**, 436 (1972).
 - ²⁸ C. Weisbuch and G. Lampel, *Solid State Communications* **14**, 141 (1974).
 - ²⁹ D. Paget, *Phys. Rev. B* **30**, 931 (1984).
 - ³⁰ V. K. Kalevich, E. L. Ivchenko, M. M. Afanasiev, A. Y. Shiryayev, A. Y. Egorov, V. M. Ustinov, B. Pal, and Y. Masumoto, *Journal of Experimental and Theoretical Physics Letters* **82**, 455 (2005).
 - ³¹ L. Lombez, P.-F. Braun, H. Carrère, B. Urbaszek, P. Renucci, T. Amand, X. Marie, J. C. Harmand, and V. K. Kalevich, *Applied Physics Letters* **87**, 252115 (2005), <https://doi.org/10.1063/1.2150252>.
 - ³² V. K. Kalevich, A. Y. Shiryayev, E. L. Ivchenko, A. Y. Egorov, L. Lombez, D. Lagarde, X. Marie, and T. Amand, *JETP Letters* **85**, 174 (2006).
 - ³³ D. Lagarde, L. Lombez, X. Marie, A. Balocchi, T. Amand, V. K. Kalevich, A. Shiryayev, E. Ivchenko, and A. Egorov, *physica status solidi (a)* **204**, 208 (2007), <https://onlinelibrary.wiley.com/doi/pdf/10.1002/pssa.200673009>.
 - ³⁴ F. Zhao, A. Balocchi, G. Truong, T. Amand, X. Marie, X. J. Wang, I. A. Buyanova, W. M. Chen, and J. C. Harmand, *Journal of Physics: Condensed Matter* **21**, 174211 (2009).
 - ³⁵ X. Wang, I. A. Buyanova, F. Zhao, D. Lagarde, A. Balocchi, X. Marie, C. Tu, J. Harmand, and W. Chen, *Nature materials* **8**, 198 (2009).
 - ³⁶ V. Kalevich, A. Shiryayev, E. Ivchenko, M. Afanasiev, A. Egorov, V. Ustinov, and Y. Masumoto, *Physica B: Condensed Matter* **404**, 4929 (2009).
 - ³⁷ H. M. Zhao, L. Lombez, B. L. Liu, B. Q. Sun, Q. K. Xue, D. M. Chen, and X. Marie, *Applied Physics Letters* **95**, 041911 (2009), <https://doi.org/10.1063/1.3186076>.
 - ³⁸ F. Zhao, A. Balocchi, A. Kunold, J. Carrey, H. Caré, T. Amand, N. Ben Abdallah, J. C. Harmand, and X. Marie, *Applied Physics Letters* **95**, 241104 (2009), <https://doi.org/10.1063/1.3273393>.
 - ³⁹ X. J. Wang, Y. Puttisong, C. W. Tu, A. J. Ptak, V. K. Kalevich, A. Y. Egorov, L. Geelhaar, H. Riechert, W. M. Chen, and I. A. Buyanova, *Applied Physics Letters* **95**, 241904 (2009), <https://doi.org/10.1063/1.3275703>.
 - ⁴⁰ Y. Puttisong, X. J. Wang, I. A. Buyanova, H. Carrère, F. Zhao, A. Balocchi, X. Marie, C. W. Tu, and W. M. Chen, *Applied Physics Letters* **96**, 052104 (2010), <https://doi.org/10.1063/1.3299015>.
 - ⁴¹ E. L. Ivchenko, V. K. Kalevich, A. Y. Shiryayev, M. M. Afanasiev, and Y. Masumoto, *Journal of Physics: Condensed Matter* **22**, 465804 (2010).
 - ⁴² A. Kunold, A. Balocchi, F. Zhao, T. Amand, N. B. Abdallah, J. C. Harmand, and X. Marie, *Phys. Rev. B* **83**, 165202 (2011).
 - ⁴³ V. K. Kalevich, M. M. Afanasiev, A. Y. Shiryayev, and A. Y. Egorov, *Phys. Rev. B* **85**, 035205 (2012).
 - ⁴⁴ C. T. Nguyen, A. Balocchi, D. Lagarde, T. T. Zhang, H. Carrère, S. Mazzucato, P. Barate, E. Galopin, J. Gierak, E. Bourhis, J. C. Harmand, T. Amand, and X. Marie, *Applied Physics Letters* **103**, 052403 (2013), <https://doi.org/10.1063/1.4816970>.
 - ⁴⁵ V. K. Kalevich, M. M. Afanasiev, A. Y. Shiryayev, and A. Y. Egorov, *JETP Letters* **96**, 567 (2013).
 - ⁴⁶ Y. Puttisong, X. Wang, I. Buyanova, L. Geelhaar, H. Riechert, A. Ptak, C. Tu, and W. Chen, *Nature communications* **4**, 1751 (2013).
 - ⁴⁷ Y. Puttisong, X. J. Wang, I. A. Buyanova, and W. M. Chen, *Phys. Rev. B* **87**, 125202 (2013).
 - ⁴⁸ C. Sandoval-Santana, A. Balocchi, T. Amand, J. C. Harmand, A. Kunold, and X. Marie, *Phys. Rev. B* **90**, 115205 (2014).
 - ⁴⁹ E. L. Ivchenko, L. A. Bakaleinikov, and V. K. Kalevich, *Phys. Rev. B* **91**, 205202 (2015).
 - ⁵⁰ E. L. Ivchenko, L. A. Bakaleinikov, M. M. Afanasiev, and V. K. Kalevich, *Physics of the Solid State* **58**, 1539 (2016).
 - ⁵¹ V. G. Ibarra-Sierra, J. C. Sandoval-Santana, S. Aza-

- izia, H. Carrère, L. A. Bakaleinikov, V. K. Kalevich, E. L. Ivchenko, X. Marie, T. Amand, A. Balocchi, and A. Kunold, *Phys. Rev. B* **95**, 195204 (2017).
- ⁵² S. Azaizia, H. Carrère, J. C. Sandoval-Santana, V. G. Ibarra-Sierra, V. K. Kalevich, E. L. Ivchenko, L. A. Bakaleinikov, X. Marie, T. Amand, A. Kunold, and A. Balocchi, *Phys. Rev. B* **97**, 155201 (2018).
- ⁵³ J. C. Sandoval-Santana, V. G. Ibarra-Sierra, S. Azaizia, H. Carrère, L. A. Bakaleinikov, V. K. Kalevich, E. L. Ivchenko, X. Marie, T. Amand, A. Balocchi, and A. Kunold, *The European Physical Journal Plus* **133**, 122 (2018).
- ⁵⁴ V. Ibarra-Sierra, J. Sandoval-Santana, S. Azaizia, H. Carrère, L. Bakaleinikov, V. Kalevich, E. Ivchenko, X. Marie, T. Amand, A. Balocchi, *et al.*, *Journal of Materials Science: Materials in Electronics* **29**, 15307 (2018).
- ⁵⁵ S. Chen, Y. Huang, D. Visser, S. Anand, I. A. Buyanova, and W. M. Chen, *Nature communications* **9**, 3575 (2018).
- ⁵⁶ F. Meier and B. P. Zakharchenya, *Optical orientation* (Elsevier, 2012).
- ⁵⁷ M. Reason, Y. Jin, H. A. McKay, N. Mangan, D. Mao, R. S. Goldman, X. Bai, and C. Kurdak, *Journal of Applied Physics* **102**, 103710 (2007), <https://doi.org/10.1063/1.2798629>.
- ⁵⁸ S. Dhar, A. Mondal, and T. D. Das, *Semiconductor Science and Technology* **23**, 015007 (2007).
- ⁵⁹ J. Ibáñez, R. Cuscó, E. Alarcón-Lladó, L. Artús, A. Patané, D. Fowler, L. Eaves, K. Uesugi, and I. Suenmune, *Journal of Applied Physics* **103**, 103528 (2008), <https://doi.org/10.1063/1.2927387>.
- ⁶⁰ H. Suzuki, T. Hashiguchi, N. Kojima, Y. Ohshita, and M. Yamaguchi, in *2009 34th IEEE Photovoltaic Specialists Conference (PVSC)* (2009) pp. 000848–000851.
- ⁶¹ M. Inagaki, K. Ikeda, H. Kowaki, Y. Ohshita, N. Kojima, and M. Yamaguchi, *physica status solidi c* **10**, 589 (2013), <https://onlinelibrary.wiley.com/doi/pdf/10.1002/pssc.201200383>.
- ⁶² A. Patané, G. Allison, L. Eaves, M. Hopkinson, G. Hill, and A. Ignatov, *Journal of Physics: Condensed Matter* **21**, 174209 (2009).
- ⁶³ J. C. Sandoval-Santana, V. G. Ibarra-Sierra, H. Carrère, M. M. Afanasiev, L. A. Bakaleinikov, V. K. Kalevich, E. L. Ivchenko, X. Marie, T. Amand, A. Balocchi, and A. Kunold, *Phys. Rev. B* **101**, 075201 (2020).
- ⁶⁴ R. K. Wangsness and F. Bloch, *Phys. Rev.* **89**, 728 (1953).
- ⁶⁵ A. Redfield, in *Advances in Magnetic Resonance*, *Advances in Magnetic and Optical Resonance*, Vol. 1, edited by J. S. Waugh (Academic Press, 1965) pp. 1 – 32.
- ⁶⁶ G. W. Leppelmeier and E. L. Hahn, *Phys. Rev.* **142**, 179 (1966).
- ⁶⁷ R. H. Masud Chaichian, *Symmetries in Quantum Mechanics: From Angular Momentum to Supersymmetry (Graduate Student Series in Physics)*, 1st ed., Graduate Student Series in Physics (Taylor & Francis, 1997).